



RESEARCH LETTER

10.1002/2015GL067369

Key Points:

- Slip is segmented along dip
- Large shallow slip efficiently generated a tsunami
- Shallow slip deficits potentially accumulate at a different rate

Supporting Information:

- Texts S1 and S2, Figures S1–S10, and Table S1

Correspondence to:

D. Melgar,
dmelgar@berkeley.edu

Citation:

Melgar, D., W. Fan, S. Riquelme, J. Geng, C. Liang, M. Fuentes, G. Vargas, R. M. Allen, P. M. Shearer, and E. J. Fielding (2016), Slip segmentation and slow rupture to the trench during the 2015, M_w 8.3 Illapel, Chile earthquake, *Geophys. Res. Lett.*, 43, 961–966, doi:10.1002/2015GL067369.

Received 9 DEC 2015

Accepted 12 JAN 2016

Accepted article online 14 JAN 2016

Published online 4 FEB 2016

Slip segmentation and slow rupture to the trench during the 2015, M_w 8.3 Illapel, Chile earthquake

Diego Melgar¹, Wenyuan Fan², Sebastian Riquelme³, Jianghui Geng⁴, Cunren Liang⁵, Mauricio Fuentes⁶, Gabriel Vargas⁷, Richard M. Allen¹, Peter M. Shearer², and Eric J. Fielding⁵

¹Seismological Laboratory, University of California, Berkeley, California, USA, ²Cecil H. and Ida M. Green Institute of Geophysics and Planetary Physics, Scripps Institution of Oceanography, University of California, San Diego, San Diego, California, USA, ³Centro Sismológico Nacional, Universidad de Chile, Santiago, Chile, ⁴GNSS Center, Wuhan University, Wuhan, China, ⁵Jet Propulsion Laboratory, California Institute of Technology, Pasadena, California, USA, ⁶Departamento de Geofísica, Universidad de Chile, Santiago, Chile, ⁷Departamento de Geología, Universidad de Chile, Santiago, Chile

Abstract The 2015 M_w 8.3 Illapel, Chile earthquake is the latest megathrust event on the central segment of that subduction zone. It generated strong ground motions and a large (up to 11 m runup) tsunami which prompted the evacuation of more than 1 million people in the first hours following the event. Observations during recent earthquakes suggest that these phenomena can be associated with rupture on different parts of the megathrust. The deep portion generates strong shaking while slow, large slip on the shallow fault is responsible for the tsunami. It is unclear whether all megathrusts can have shallow slip during coseismic rupture and what physical properties regulate this. Here we show that the Illapel event ruptured both deep and shallow segments with substantial slip. We resolve a kinematic slip model using regional geophysical observations and analyze it jointly with teleseismic backprojection. We find that the shallow and deep portions of the megathrust are segmented and have fundamentally different behavior. We forward calculate local tsunami propagation from the resolved slip and find good agreement with field measurements, independently validating the slip model. These results show that the central portion of the Chilean subduction zone has accumulated a significant shallow slip deficit and indicates that, given enough time, shallow slip might be possible everywhere along the subduction zone.

1. Motivation

The Chilean subduction zone is seismically very active. Since 1906, it has produced 10 large ($8 < M_w < 8.5$) and 3 very large ($M_w > 8.5$) events on its central part (26°S to 38°S), the seismic history is well documented dating back to the eighteenth century [Beck *et al.*, 1998; Lomnitz, 2004] (Figure 1). The 2015 M_w 8.3 Illapel earthquake is the most recent event on this segment. There was strong ground shaking, with accelerations reaching up to 98% of gravity, or Mercalli intensity IX (violent shaking) (Figure S1 in the supporting information), which was widely reported throughout the source region. One million people were evacuated in the low-lying coastal areas of Chile in the first hour after the event [Melgar *et al.*, 2016]; the earthquake produced a tsunami as high as 11 m in the near-source region (Figure 2).

The Illapel event is the largest earthquake in the area since the 2010 M_w 8.8 Maule earthquake 350 km to the south [Vigny *et al.*, 2011]. Prior to this, the 1943 M_w 8.2 and the 1971 M_w 7.5 events (<http://www.sismologia.cl/>) ruptured this same approximate section of the megathrust and the 1922 M_w 8.5 event ruptured a 350 km segment just north and produced a substantial (~9 m) tsunami [Beck *et al.*, 1998; Lomnitz, 2004]. Here we present a detailed study of the source kinematics. We posit that, along dip, the megathrust is segmented into at least two domains in this region, with different seismic properties. Furthermore, the results indicate that a shallow slip deficit could be accumulated elsewhere on the megathrust with important implications for tsunami hazards.

2. Data and Methods

We use two approaches to investigate the earthquake. First, we resolve a kinematic source model by jointly inverting a variety of regional geophysical observables: nine 3-component high-rate GPS records, nine 3-component strong motion records, two interferograms from ascending and descending passes of the Sentinel-1A satellite, and 7 tide gauge records (Figures 1, S2, and S3 and Text S1). The GPS data are absolute positions estimates obtained with the precise point-positioning algorithm with ambiguity resolution of Geng

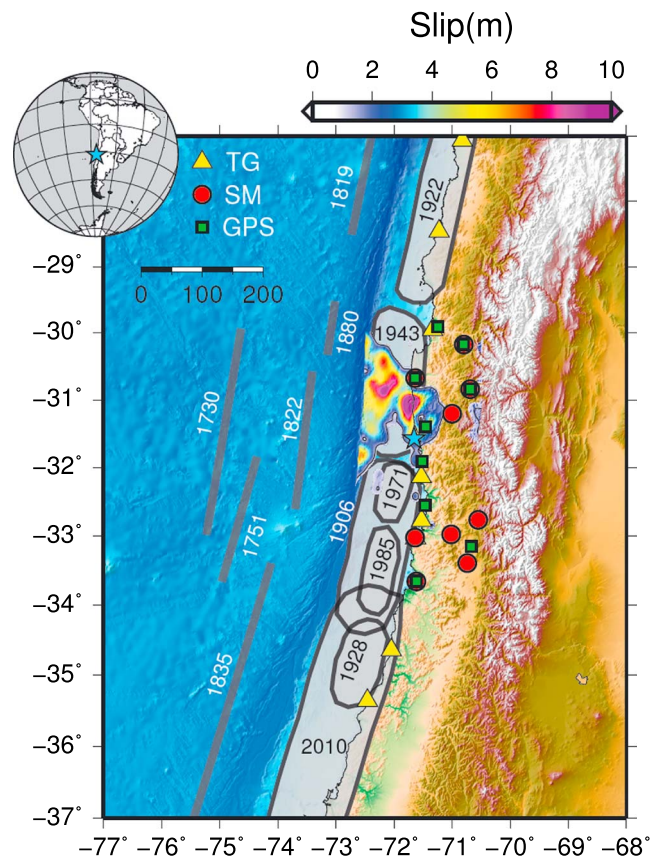


Figure 1. Large historical earthquakes and the 2015 M_w 8.3 Illapel earthquake. Grey shaded areas are the approximate source areas of large events from aftershock zones of the twentieth and twenty-first centuries. Thick black lines denote the approximate extent of older events from historical evidence [Beck *et al.*, 1998; Lomnitz, 2004]. The color pattern is the total slip from the kinematic inversion of tide gauge (TG), strong motion (SM), high-rate GPS stations, and Sentinel-1A InSAR (Figures S2 and S3) data for the Illapel earthquake. The event epicenter is denoted by the blue star.

et al. [2013]. The slip inversion uses the open-source MudPy code [Melgar and Bock, 2015] that employs the multi-time window method and uses a 1-D layered Earth velocity model and a 3-D fault geometry (Text S2). Combining diverse observations is essential for obtaining a model with high resolution at both the deep and shallow parts of the megathrust [Melgar and Bock, 2015]. This is further exemplified by a checkerboard test (Figure S4), which shows that the time-dependent waveforms (GPS and strong motion) have overall similar sensitivity to the entire fault model. However, the tide gauge data have very high resolution for the offshore portions while the interferometric synthetic aperture radar (InSAR) static offsets have excellent resolution for the deeper, onshore portion. The combination of all four data sets provides optimal resolution. We further validate the kinematic source inversion by using it to forward calculate a local tsunami propagation model [Melgar and Bock, 2013] and comparing the model predictions to the runups measured at 28 locations (Table S1). Along the rupture region, the survey-measured tsunami heights are in areas directly exposed to the open ocean [Sugawara *et al.*, 2008]. We observed the highest pervasive marks left by vegetation razed by the tsunami and traces of erosion on the beach, sand, and boulder deposits as well as the effect on coastal localities. To estimate tsunami heights with respect to sea level the measurements were corrected for tides according to tidal heights reported by the Chilean Navy Hydrographic and Oceanographic Service (SHOA, www.shoa.cl). We used a 1 m precision barometric altimeter, calibrated at the moment of each measurement; we assigned an error of ± 0.5 m to these observations.

In addition to the finite-fault inversion, we backproject 452 far-field broadband P wave records (Figure 2 and Text S2) from Central and North America to image the spatiotemporal evolution of the earthquake [Ishii *et al.*, 2005; Walker *et al.*, 2005], using two frequency bands, low frequency (LF, 0.02–0.5 Hz) and high frequency (HF, 0.5–2 Hz), to investigate potential frequency-dependent rupture behavior [Fan and Shearer, 2015]

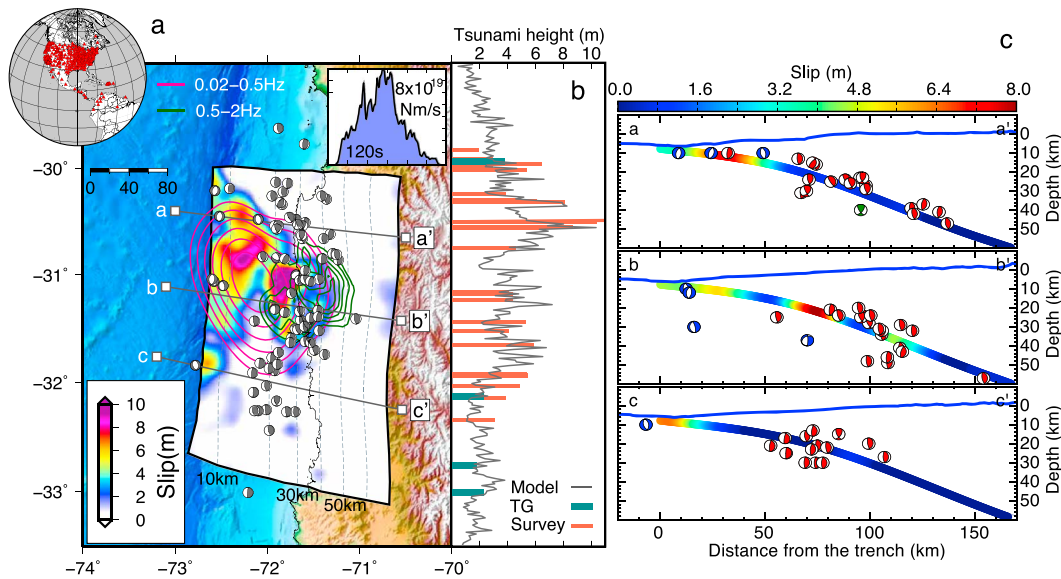


Figure 2. Correlation between slip, time-integrated backprojection contours, and aftershock moment tensors. (a) The slip inversion results of Figure 1 compared to the backprojection (BP) results. The contours are normalized time-integrated backprojection images from 50 to 100% for high frequency (HF) and from 70 to 100% for low frequency (LF). The green lines are the HF BP and the red contours are LF BP results showing correlation with the shallow slip. The red triangles are the 452 stations used in the BP. Plotted are the moment tensors of 3 weeks of aftershocks between $M_w 4.3$ and $M_w 7$ [GEOFON, 2015]. The dashed lines are depth contours for the assumed fault surface at 10 km intervals [Hayes *et al.*, 2012]. The inset is the source time function for the slip inversion, the total duration is 120 s, and peak moment rate is 8×10^{19} N m s (b) Comparison between the tsunami amplitude predicted by the slip inversion (grey) and the field survey measurements (orange) and maximum amplitudes (blue) at local tide gauges. (c) Depth cross section showing slip on the assumed fault geometry and the positions of the aftershock moment tensors. Lower hemisphere projections are shown, red moment tensors are thrust, blue are normal, and green are oblique faulting mechanisms.

(Figure S5). Using a combination of these near-field and far-field observations, we obtain detailed constraints on the source process and a comprehensive view of the underlying fault properties.

3. Results

The results are summarized in Figure 2. In the along-dip direction, the slip is segmented into two domains, roughly split at the 20 km depth contour. The “deep” asperity, north of the hypocenter, is well separated from the “shallow” asperity by a gap of reduced slip. The deep slip patch extends to 45 km depth, with ~10 m peak slip at ~30 km depth. The shallow slip patch ruptured all the way to the trench, with ~10 m peak slip at ~15 km. The shallow rupture spanned ~200 km along strike, with ~5 m displacement near the trench, in contrast to the compact rupture of the deep asperity. The integrated backprojection (BP) images over 120 s correlate well with the finite-fault slip model and show clear frequency-dependent rupture behavior. Most of the HF energy was released downdip, while the majority of LF energy was released updip close to the slip-centroid location. The HF energy burst collocates with the deep asperity, contouring the deeper slip edge between 30 and 45 km, but shows little power above 20 km depth. The integrated LF energy burst is well separated from the HF energy burst, overlapping with the shallow rupture area imaged by the slip inversion. There is substantial near-trench seismic radiation evidenced by the LF backprojection, independently validating the observed shallow slip in the finite-fault model.

The resolved kinematic slip model is anticorrelated with the distribution of 3 weeks of aftershocks [GEOFON, 2015] (86 events, $M_w 4.3-7$, Figures 2a and 2c). At least five aftershocks show high-angle normal faulting close to the trench and bracket the area of large shallow slip. These events potentially indicate trench-slope faulting as a result of large shallow slip on the megathrust [Lay *et al.*, 2012]. Most of the aftershocks (77) share low-angle thrust faulting mechanisms with strikes and dips consistent with the megathrust geometry. These thrust aftershocks are concentrated largely at depths greater than ~15 km and down to ~45 km. There is a notable dearth of postevent seismicity in the shallow megathrust between the trench and ~15 km depth, with only a single thrust event, even though there was significant slip in this shallow segment during the main shock.

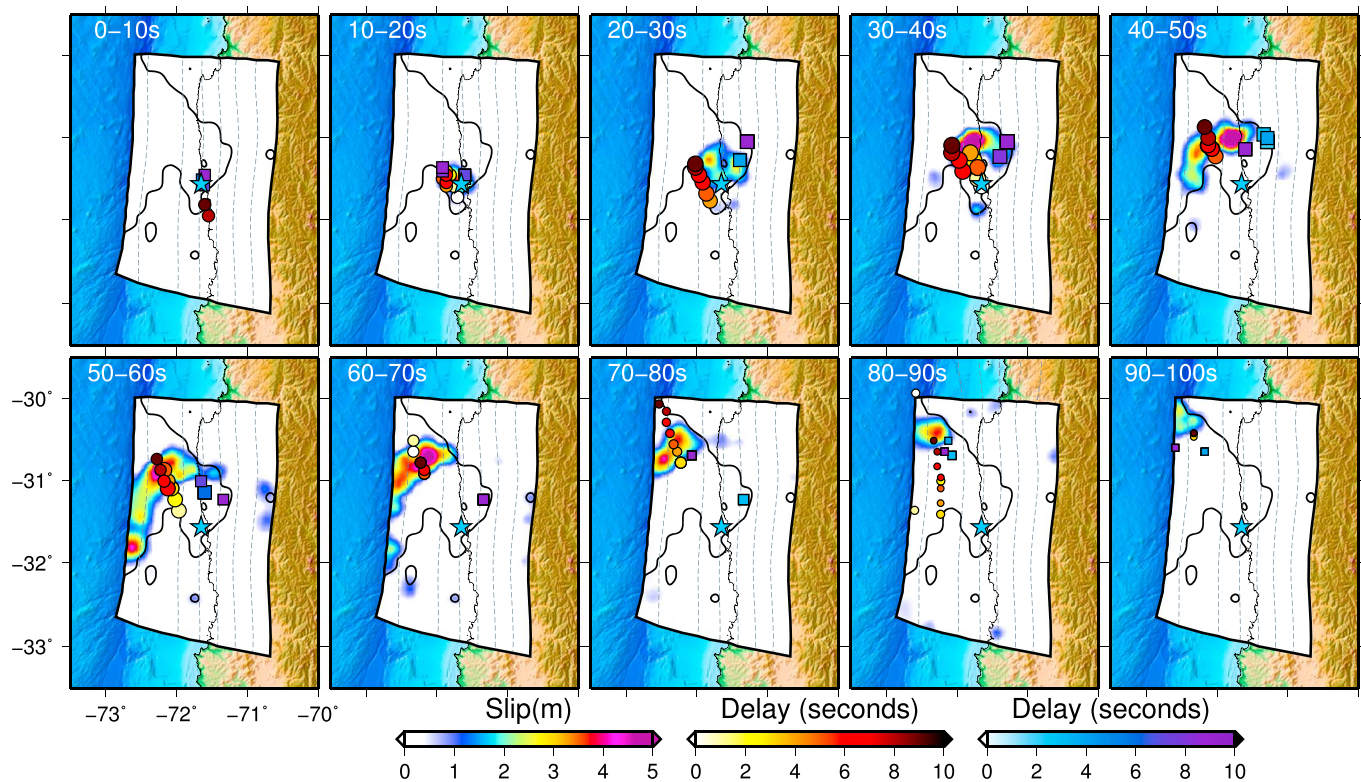


Figure 3. Rupture evolution revealed by the slip inversion and back projection techniques. Ten second snapshots of the slip inversion; the thick black line is the 1 m slip contour which outlines where the majority of slip happens. Loci of the peak beam power of the backprojection are plotted at 1 s intervals on each snapshot. The circles are the low-frequency backprojection and the squares the high-frequency backprojection. The color of each symbol represents the time delay within each snapshot time window at which the peak power is achieved and the size of the symbol scales in relation to the peak beam power. The blue star denotes the event epicenter, and dashed lines are the depth to the slab at 10 km intervals.

The multi-time window inversion method (Text S2) we have used for the slip inversion requires setting a maximum allowable rupture velocity. After selecting a suitable spatial regularization we tested several values of maximum rupture speed and studied the effects of this parameter on the data fits. The results (Figure S6) show that the fit to the different data sets is best when a slow rupture speed of 1.8–2.0 km/s is used; we selected 2.0 km/s as the preferred rupture speed. The time evolution of the rupture model at this slow rupture speed is plotted in Figure 3 and shows detailed features of the event kinematics. The earthquake began with unilateral rupture to the north, extending from the hypocenter at 30 km depth in the updip and downdip directions. Downdip rupture arrests at ~40 s after the event origin time (OT) and at 45 km depth but then continues updip for another full minute. The shallow slip west of the hypocenter is separated from the deep slip by a gap of reduced slip. On this shallow slip patch, rupture grows bilaterally along strike producing significant slip of up to 8 m all the way to the trench.

This rupture evolution model is supported by the backprojection snapshot results (Figure 3), with different behavior seen in different frequency bands. The high-frequency BP tracks the initial growth of the rupture front both updip and downdip from the hypocenter until about 50 s after OT and up to ~25 km depth. High-frequency BP power at shallow depths is very weak, in contrast to the low-frequency BP that tracks the rupture front coherently all the way to the trench. The low-frequency BP cannot resolve the bilateral near-trench slip in the slip model. The rupture propagation from BP tracks the northern branch of the shallow slip where the largest slip occurs (Figure S7). From 80 to 90 s, LF BP snapshots indicate a possible delayed (~20 s) rupture south of the slip patch resolved in the slip inversion. Similar delays have been observed from tsunami-only inversion of the 2011 M_w 9.0 Tohoku-oki earthquake [Satake *et al.*, 2013].

A large tsunami resulted from the coseismic slip. The survey shows two areas of maximum tsunami amplitude, one reaching ~6 m just to the south of the epicenter and the other reaching as high as ~11 m (Figure 2b), to the north of the epicenter. First arrivals reached the coast ~5–7 min after the start of shaking, according to witnesses

along the epicentral zone. With a peak amplitude of ~ 11 m, the tsunami is comparable in peak amplitude to that of the 2010 $M_w 8.8$ Maule earthquake, albeit with a more limited geographical extent [Fritz *et al.*, 2011; Vargas *et al.*, 2011]. The good agreement between the predicted local tsunami amplitudes to field survey measurements validates the presence of the large shallow slip predicted by the slip inversion (Figure 2b).

4. Discussion

The resolved kinematic slip model, in conjunction with the aftershock locations, agrees with the concept of along-dip segmentation of the megathrust properties [Lay *et al.*, 2012; Yao *et al.*, 2013]. If rupture had occurred only within what is traditionally thought of as the seismogenic zone, as defined by where there are large thrust aftershocks and where there is ample catalogue seismicity (Figures 2c and S8, ~ 15 to 45 km depth), the deep asperity for this event would produce a $M_w 7.5$ – 8 earthquake similar to the $M_w 7.5$ 1971 or $M_w 8.0$ 1985 (Figure 1) events. This rupture scenario is analogous to what was observed further north during the 2014 Iquique $M_w 8.1$ earthquake [Hayes *et al.*, 2014], which had ample high-frequency energy and resulted in substantial strong motions. Earthquakes with no shallow slip are expected to be depleted in long-period radiation [Lay *et al.*, 2012] and produce only modest, if any, tsunamis; indeed this was the case for the Iquique event [Gusman *et al.*, 2015]. In contrast, the megathrust above ~ 15 km depth behaves differently from the seismogenic segment. Notably, it also has substantially less catalogue seismicity (Figure S8). Furthermore, the paucity of aftershocks in this region is striking, in spite of the large loading from the substantial coseismic slip. The dearth of coseismic high-frequency radiation (Figure 2) contrasts markedly from the observations from the deeper segment. It has been hypothesized that plate coupling in this shallow region could be high, but the resolution of these models, based entirely on land-based GPS measurements is low offshore [Métis *et al.*, 2012] and as a result the shallow pattern of coupling is very sensitive to model inversion regularization. It is possible that reduced coupling in the shallow megathrust results in the shallow portion accumulating significantly less strain.

Similarly, had only the shallow segment broken, this would have been a “tsunami” earthquake [Lay *et al.*, 2012], an earthquake with a large tsunamigenic component but little strong motion due to the lack of slip on the deeper portion of the megathrust [e.g., Hill *et al.*, 2012]. Such shallow events with high-frequency energy depletion have not been observed in Chile, but only limited historical records are available. The southern part of the megathrust that hosted the 1960 $M_w 9.5$ and 2010 $M_w 8.8$ events has well documented paleotsunamis [Cisternas *et al.*, 2005] but in the central segment the history is not so clear. The tsunami during the $M_w 8.5$ 1922 earthquake to the north was estimated to have a maximum amplitude of 7–9 m [Beck *et al.*, 1998] but was accompanied by widespread strong shaking. Additionally, tsunamis from other historical events in the last 500 years on the central subduction zone, (including the $M_w 8.2$ 1943 Illapel event) have been no larger than ~ 4 m [Beck *et al.*, 1998; Dura *et al.*, 2015]. The more recent 1971 ($M_w 7.5$) and 1985 ($M_w 8.0$) events produced strong shaking and very little tsunami excitation [Comte *et al.*, 1986].

These observations can be collectively interpreted to suggest that in the central subduction zone of Chile, strain accumulation at the shallow megathrust is occurring but at a rate significantly slower than the interseismic plate convergence of 72 mm/yr [Vigny *et al.*, 2009]. Assuming the 1943 event ruptured both the shallow and deep segments, the preevent slip deficit on the shallow megathrust would be at no more than ~ 5 m of accumulated slip (assuming perfect coupling) [Métis *et al.*, 2012]. The large shallow slip of up to 10 m and lack of tsunami excitation during the 1943 earthquake suggests that in 1943 only the deeper seismogenic segment ruptured. Furthermore, substantial deep slip observed in the 2015 event indicates that it is likely that slip occurred only along the deep northern section of the 1943 aftershock area indicated in Figure 1. The lack of large historical tsunamis suggests that most earthquakes in this region only rupture the seismogenic zone and do not efficiently excite tsunami waves. Strain at the shallow segment accumulates at a substantially slower rate and is released only infrequently.

In many respects, the Illapel event resembles a smaller-scale version of the 2011 $M_w 9.0$ Tohoku-oki event. The deep portion of the earthquake generated substantial high-frequency energy that led to strong motions throughout the epicentral zone. The earthquake ruptured the shallow portion of the megathrust at a very slow velocity, produced little high-frequency energy updip, ruptured all the way to the trench with large slip, and efficiently generated tsunami waves. Whether this is the only mode by which shallow strain is released in the shallow portion of the megathrust is unclear, but the lack of historical “tsunami events” suggests that rupture does not nucleate in the shallow portion of this segment of the megathrust.

5. Conclusions

We analyzed the kinematic source characteristics of the 2015 M_w 8.3 Illapel earthquake by comparing the results of a kinematic slip inversion from regional geophysical data and teleseismic P wave back projection on two frequency bands. Two large slip patches are observed with one ~ 10 m peak slip at ~ 30 km depth, and the other ~ 10 m peak slip at ~ 15 km. Backprojection results suggest frequency-dependent rupture behavior associated with the two large slip patches. The results indicated that while both the shallow and deep portions of the megathrust ruptured with significant slip they are segmented and have fundamentally different behavior. The shallow portion shows significant depletion of high-frequency radiation but efficiently generates a large tsunami (11 m+) as demonstrated by field survey measurements. The deep portion is substantially enriched in high-frequency energy generating substantial strong motions. These results show that the central portion of the Chilean subduction zone has accumulated a significant shallow slip deficit and indicates that shallow slip might be possible everywhere along the subduction zone given time for it to accumulate sufficient strain.

Acknowledgments

The teleseismic seismic data were provided by the Data Management Center (DMC) of the Incorporated Research Institutions for Seismology (IRIS). Local seismic and geodetic data are provided by the Centro Sismológico Nacional (CSN) and are available upon request. Tide gauges are operated by the Servicio Hidrográfico Oceanográfico de la Armada de Chile (SHOA) and data is available at <http://www.ioc-sealevel-monitoring.org/>. Sentinel-1 interferograms are derived works of Copernicus data. Original Sentinel-1 data is available from ESA and processed interferograms are available from the UNAVCO InSAR archive (<https://winsar.unavco.org/portal/insar/>). We extend our thanks to Roland Burgmann and Marcelo Vargas for helpful discussions and Piyush Agram for use of the prototype Sentinel-1 TOPS processing programs. We are indebted to J. Gonzalez and A. Villalobos for field support. We thank two anonymous reviewers for constructive critiques which improved the content and presentation of this manuscript. This research was funded by the Gordon and Betty Moore Foundation through grant GBMF3024 to UC Berkeley. Funding at the Scripps Institution of Oceanography is through National Science Foundation grant EAR-1111111. Part of this research was supported by the NASA Earth Surface and Interior program and performed at the Jet Propulsion Laboratory with support for an appointment to the NASA Postdoctoral Program, California Institute of Technology.

References

- Beck, S., S. Barrientos, E. Kausel, and M. Reyes (1998), Source characteristics of historic earthquakes along the central Chile subduction zone, *J. South Am. Earth Sci.*, *11*(2), 115–129.
- Cisternas, M., et al. (2005), Predecessors of the giant 1960 Chile earthquake, *Nature*, *437*, 404–407.
- Comte, D., A. Eisenberg, E. Lorca, M. Pardo, L. Ponce, R. Saragoni, S. K. Singh, and G. Suárez (1986), The 1985 central Chile earthquake: A repeat of previous great earthquakes in the region?, *Science*, *233*, 449–453.
- Dura, T., M. Cisternas, B. P. Horton, L. L. Ely, A. R. Nelson, R. L. Wesson, and J. E. Pilarczyk (2015), Coastal evidence for Holocene subduction-zone earthquakes and tsunamis in central Chile, *Quat. Sci. Rev.*, *113*, 93–111.
- Fan, W., and P. Shearer (2015), Detailed rupture imaging of the 25 April 2015 Nepal earthquake using teleseismic P waves, *Geophys. Res. Lett.*, *42*, 5744–5752, doi:10.1002/2015GL064587.
- Fritz, H. M., et al. (2011), Field survey of the 27 February 2010 Chile tsunami, *Pure Appl. Geophys.*, *168*, 1989–2010.
- Geng, J., Y. Bock, D. Melgar, B. W. Crowell, and J. S. Haase (2013), A new seismogeodetic approach applied to GPS and accelerometer observations of the 2012 Brawley seismic swarm: Implications for earthquake early warning, *Geochem. Geophys. Geosyst.*, *14*, 2124–2142, doi:10.1002/ggge.20144.
- GEOFON (2015), The 2015-09-16 M_w 8.2 earthquake and aftershocks in Central Chile. [Available at <http://geofon.gfz-potsdam.de/eqinfo/special/gfz2015sfd/>].
- Gusman, A. R., S. Murotani, K. Satake, M. Heidarzadeh, E. Gunawan, S. Watada, and B. Schurr (2015), Fault slip distribution of the 2014 Iquique, Chile, earthquake estimated from ocean-wide tsunami waveforms and GPS data, *Geophys. Res. Lett.*, *42*, 1053–1060, doi:10.1002/2014GL062604s.
- Hayes, G. P., D. J. Wald, and R. L. Johnson (2012), Slab1.0: A three-dimensional model of global subduction zone geometries, *J. Geophys. Res.*, *117*, B01302, doi:10.1029/2011JB008524.
- Hayes, G. P., et al. (2014), Continuing megathrust earthquake potential in Chile after the 2014 Iquique earthquake, *Nature*, *512*, 295–298.
- Hill, E. M., et al. (2012), The 2010 M_w 7.8 Mentawai earthquake: Very shallow source of a rare tsunami earthquake determined from tsunami field survey and near-field GPS data, *J. Geophys. Res.*, *117*, B06402, doi:10.1029/2012JB009159.
- Ishii, M., P. M. Shearer, H. Houston, and J. E. Vidale (2005), Extent, duration and speed of the 2004 Sumatra-Andaman earthquake imaged by the Hi-net array, *Nature*, *435*, 933–936.
- Lay, T., H. Kanamori, C. J. Ammon, K. D. Koper, A. R. Hutko, L. Ye, H. Yue, and T. M. Rushing (2012), Depth-varying rupture properties of subduction zone megathrust faults, *J. Geophys. Res.*, *117*, B04311, doi:10.1029/2011JB009133.
- Lomnitz, C. (2004), Major earthquakes of Chile: A historical survey, 1535–1960, *Seismol. Res. Lett.*, *75*, 368–378.
- Melgar, D., and Y. Bock (2013), Near-field tsunami models with rapid earthquake source inversions from land- and ocean-based observations: The potential for forecast and warning, *J. Geophys. Res. Solid Earth*, *118*, 5939–5955, doi:10.1002/2013JB010506.
- Melgar, D., and Y. Bock (2015), Kinematic earthquake source inversion and tsunami runup prediction with regional geophysical data, *J. Geophys. Res. Solid Earth*, *120*, 3324–3349, doi:10.1002/2014JB011832.
- Melgar, D., et al. (2016), Local tsunami warnings: Perspectives from recent large events, *Geophys. Res. Lett.*, doi:10.1002/2015GL067100.
- Metois, M., A. Socquet, and C. Vigny (2012), Interseismic coupling, segmentation and mechanical behavior of the central Chile subduction zone, *J. Geophys. Res.*, *117*, B03406, doi:10.1029/2011JB008736.
- Satake, K., Y. Fujii, T. Harada, and Y. Namegaya (2013), Time and space distribution of coseismic slip of the 2011 Tohoku earthquake as inferred from tsunami waveform data, *Bull. Seismol. Soc. Am.*, *103*, 1473–1492.
- Sugawara, D., K. Minoura, and F. Imamura (2008), Tsunamis and tsunami sedimentology, in *Tsunamiites*, edited by T. Shiki et al., pp. 9–49, Elsevier, Amsterdam.
- Vargas, G., M. Farias, S. Carretier, A. Tassara, S. Baize, and D. Melnick (2011), Coastal uplift and tsunami effects associated to the 2010 M_w 8.8 Maule earthquake in Central Chile, *Andean Geol.*, *38*(1), 219–238.
- Vigny, C., A. Rudloff, J. C. Ruegg, R. Madariaga, J. Campos, and M. Alvarez (2009), Upper plate deformation measured by GPS in the Coquimbo Gap, Chile, *Phys. Earth Planet. Inter.*, *175*(1), 86–95.
- Vigny, C., et al. (2011), The 2010 M_w 8.8 Maule megathrust earthquake of Central Chile, monitored by GPS, *Science*, *332*, 1417–1421.
- Walker, K. T., M. Ishii, and P. M. Shearer (2005), Rupture details of the 28 March 2005 Sumatra M_w 8.6 earthquake imaged with teleseismic P waves, *Geophys. Res. Lett.*, *32*, L24303, doi:10.1029/2005GL024395.
- Yao, H., P. M. Shearer, and P. Gerstoft (2013), Compressive sensing of frequency-dependent seismic radiation from subduction zone megathrust ruptures, *Proc. Natl. Acad. Sci. U.S.A.*, *110*, 4512–4517.